

# SplatCo: Structure-View Collaborative Gaussian Splatting for Detail-Preserving Rendering of Large-Scale Unbounded Scenes

Haihong Xiao, Jianan Zou, Yuxin Zhou, Ying He, Wenxiong Kang

*Abstract*—Neural Radiance Fields (NeRFs) have achieved impressive results in novel view synthesis but are less suited for large-scale scene reconstruction due to their reliance on dense per-ray sampling and deep MLP inference, which limits scalability and efficiency. In contrast, 3D Gaussian Splatting (3DGS) offers a more efficient alternative to computationally intensive volume rendering, enabling faster training and real-time rendering. Although recent efforts have extended 3DGS to large-scale settings, these methods often struggle to balance global structural coherence with local detail fidelity, and suffer from view-dependent artifacts and geometric inconsistencies, especially in sparsely observed regions. To address these challenges, we present SplatCo, a structure-view collaborative Gaussian splatting framework for high-fidelity rendering of complex outdoor environments. SplatCo builds upon two novel components: (1) a cross-structure collaboration module that combines global tri-plane representations, which capture coarse scene layouts, with local context grid features that represent fine surface details. This fusion is achieved through a novel hierarchical compensation strategy, ensuring both global consistency and local detail preservation; and (2) a cross-view assisted training strategy that enhances multi-view consistency by synchronizing gradient updates across viewpoints, applying visibility-aware densification, and pruning overfitted or inaccurate Gaussians based on structural consistency. Through joint optimization of structural representation and multi-view coherence, SplatCo effectively reconstructs fine-grained geometric structures and complex textures in large-scale scenes. Comprehensive evaluations on 13 diverse large-scale scenes, including Mill19, MatrixCity, Tanks & Temples, WHU, and custom aerial captures, demonstrate that SplatCo consistently achieves higher reconstruction quality than state-of-the-art methods, with PSNR improvements of 1–2 dB and SSIM gains of 0.1 to 0.2. These results establish a new benchmark for high-fidelity rendering of large-scale unbounded scenes. Code and additional information are available at <https://github.com/SCUT-BIP-Lab/SplatCo>.

*Index Terms*—3DGS, real-time rendering, large-scale unbounded scenes, detail preservation, structure-view collaborative learning.

## I. INTRODUCTION

NEURAL scene representations have significantly advanced novel view synthesis and 3D reconstruction. Among them, Neural Radiance Fields (NeRF) [1] achieve impressive photorealistic rendering of objects and small-scale scenes from multi-view captures, supporting applications in augmented/virtual reality [2], autonomous driving [3], digital

twins [4], telepresence [5], and cultural heritage preservation [6].

Applying NeRFs to large-scale outdoor and urban environments remains difficult due to both computational and representational challenges. These scenes are typically unbounded, which introduces numerical instability in volume rendering. NeRF’s reliance on dense per-ray sampling and deep MLP inference leads to high computational cost, limiting scalability. In addition, NeRFs have limited capacity to model extended spatial regions, often resulting in blurred geometry and textures. Per-view training can also cause single-view overfitting, where reconstructions conform too closely to individual camera rays. This issue becomes more pronounced in sparsely observed areas and reduces consistency across views. Finally, there is a fundamental trade-off between global and local representations: global factorizations capture coarse structure but miss surface detail, while local grids better preserve detail but may become misaligned without a consistent global frame.

To overcome these limitations, 3D Gaussian Splatting (3DGS) [7] has emerged as an efficient alternative. It represents a scene as a sparse collection of anisotropic 3D Gaussians whose positions, shapes, orientations, and colors are optimized directly from images. These Gaussians are rendered using a tile-based GPU splatting pipeline, enabling high-quality, real-time rendering.

While 3DGS addresses many of the efficiency and scalability issues inherent in NeRF, extending it to large-scale environments introduces new challenges related to structure preservation, detail fidelity, and multi-view consistency. Several strategies have been proposed to scale 3DGS to campus- or city-scale scenes. Tri-plane factorization [8], [9] compresses 3D structure into three orthogonal feature planes, which efficiently capture global layout. However, this representation tends to blur or omit fine surface details, particularly along curved or oblique regions not aligned with the coordinate axes. Context-grid augmentations [10], [11] divide the scene into local voxel grids to recover high-frequency detail. Yet, covering large spatial extents incurs substantial memory and computational overhead. Without a shared global structure, neighboring tiles may drift out of alignment, resulting in inconsistent geometry. Octree hierarchies [12] adaptively allocate capacity to complex regions by subdividing space, but the lack of mechanisms for enforcing consistency across views and scales often causes popping artifacts, missing geometry in under-observed zones, or redundant Gaussians in areas with dense coverage.

Haihong Xiao, Jianan Zou, Yuxin Zhou, Ying He and Wenxiong Kang (e-mail: auhhxiao@mail.scut.edu.cn; 202130450216@mail.scut.edu.cn; 202164690558@mail.scut.edu.cn; yhe@ntu.edu.sg; auwxkang@scut.edu.cn).

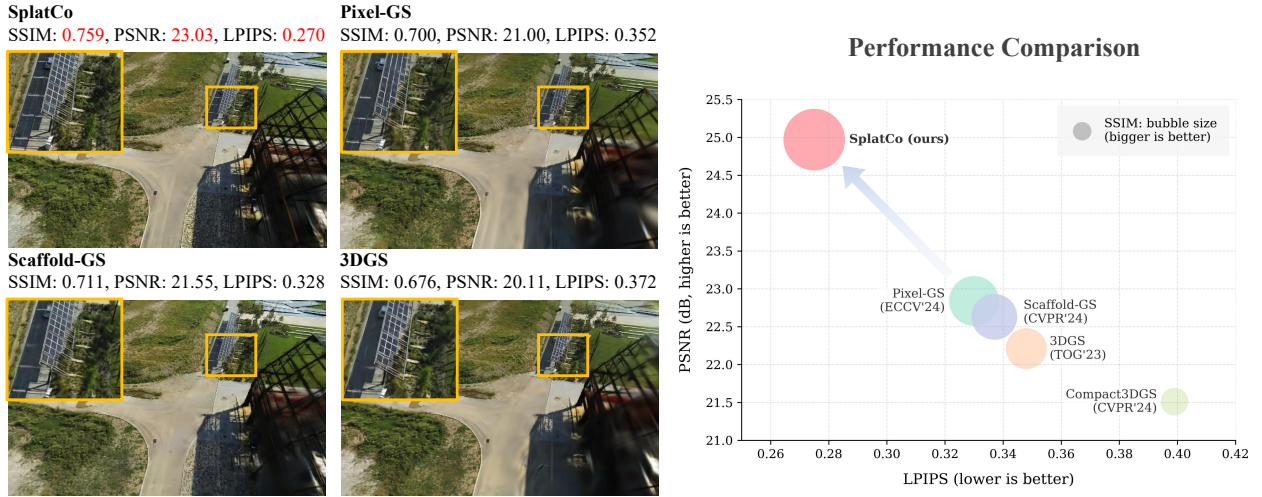


Fig. 1. Comparison of 3DGS-based methods on two scenes (Rubble and Building) from the Mill-19 Dataset. Yellow squares highlight regions with noticeable visual differences. SplatCo produces more realistic and detailed renderings, recovering sharper texture patterns compared to state-of-the-art methods. The chart on the right presents quantitative results across three standard rendering metrics: PSNR, SSIM and LPIPS.

In this work, we propose Structure-View Collaborative Gaussian Splatting (SplatCo), a unified framework for high-fidelity reconstruction and rendering of large-scale outdoor scenes. Unlike prior approaches that separately address geometry representation or view consistency, SplatCo integrates both global structure modeling and multi-view coherence into a single, jointly optimized system. First, we incorporate multi-scale contextual information into a global tri-plane backbone using a three-level compensation mechanism, which aligns coarse scene layout with detailed local geometry and texture. Second, to maintain consistency across viewpoints, we synchronize gradient updates across overlapping views, ensuring coherent Gaussian positioning and appearance. Third, we introduce a visibility-aware optimization process that densifies sparsely observed regions while removing overfitted or inconsistent Gaussians based on structural consistency. By combining these components in a unified training and inference pipeline, SplatCo achieves robust generalization and fine-detail reconstruction across complex, large-scale environments, as shown in Fig. 1.

We validate SplatCo on 13 large-scale outdoor scenes, including four public benchmarks (Mill-19, MatrixCity, Tanks & Temples, WHU) and five custom aerial captures. Compared to state-of-the-art Gaussian-based methods, SplatCo consistently improves PSNR by 1–2 dB and SSIM by 0.1–0.2, demonstrating its effectiveness in high-fidelity rendering of unbounded outdoor environments.

Our main contributions are as follows:

- We propose a cross-structure collaboration module that combines global tri-plane features with local context grids through a hierarchical compensation mechanism, enabling both fine detail preservation and globally consistent geometry.
- We introduce a cross-view assisted training strategy that synchronizes gradient updates across overlapping views, reducing single-view overfitting and improving multi-view consistency in large-scale scenes.

- We develop a structural-consistency-guided pruning mechanism that removes over-specialized Gaussians, enhancing geometric integrity and reducing redundancy.
- We conduct extensive experiments on diverse large-scale outdoor scenes, showing that SplatCo achieves state-of-the-art performance in detail-preserving novel view synthesis.

## II. RELATED WORK

### A. Multi-view 3D Reconstruction

3D reconstruction has long been a central problem in computer vision, with many approaches relying on multi-view image inputs to infer scene geometry. Structure-from-Motion (SfM) [13], [14] approaches rely on handcrafted features, such as SIFT [15]), and bundle adjustment [16] to recover sparse scene structures. Multi-View Stereo (MVS) [17], [18] methods extend these techniques by estimating dense depth maps across multiple views, thereby producing detailed point clouds. These raw point clouds can be fed into point orientation methods, such as [19]–[22], to compute globally consistent orientations. Meshes can be constructed from the oriented point clouds using surface reconstruction techniques such as Poisson surface reconstruction [23], [24].

Learning-based MVS methods [25]–[30] have demonstrated significant improvements in reconstruction accuracy and robustness by adopting a standardized four-stage pipeline: (1) feature extraction, (2) differentiable homography, (3) cost volume regularization, and (4) depth map regression. Variants have improved speed and scalability using recurrent networks [27], coarse-to-fine cascades [28], and Transformer backbones [29]. More compact and flexible depth representations have also been explored [30]. However, cost volumes are memory-intensive and resolution-limited, making these methods less practical for real-time or outdoor-scale reconstruction.

Recently, feature-matching-based approaches, such as DUST3R [31] and its variants [32]–[34], further reduce reliance on depth volumes by directly matching features across

images. These methods offer a promising alternative for scalable reconstruction.

### B. Novel View Synthesis

Novel view synthesis has become a central task in visual computing, with broad relevance to virtual and augmented reality, robotics, and autonomous systems. Early work used explicit representations, such as meshes [35], [36], voxels [37], [38], and point clouds [39], to model scenes. However, these methods struggled to reproduce fine visual details.

Neural Radiance Fields (NeRF) [1] introduced a view-consistent rendering framework based on implicit volumetric representations learned from 2D images. While NeRF produces realistic results in controlled scenes, its sampling inefficiency and reliance on large MLPs lead to slow training and inference. These issues are especially pronounced in outdoor or large-scale environments. To improve performance, various acceleration methods have been proposed [40], [41], along with anti-aliasing [42], [43], motion deblurring [44], [45], and support for dynamic content [46]. However, the fundamental design of NeRF still poses scalability and efficiency challenges.

3D Gaussian Splatting [7] offers a more efficient rendering pipeline by replacing volume sampling with rasterization and representing the scene as a set of Gaussian primitives. This design enables real-time rendering with competitive visual quality and has become the basis for a growing body of recent work.

### C. 3D Gaussian Splatting for Large-Scale Scenes

3DGS has been widely adopted for modeling objects and scenes due to its speed and rendering quality. Readers may refer to recent surveys for comprehensive overviews of 3DGS and its applications [47]–[49]. While early applications focused on compact scenes, such as individual objects [50], [51], humans [52]–[54], and indoor environments [55]–[57], adapting 3DGS to large-scale outdoor scene remains a challenge.

To bridge this, recent works propose scalable variants. Scaffold-GS [58] introduces a hierarchical, region-aware 3D representation via anchor points. DOGS [59] significantly improves training efficiency through a distributed paradigm that combines spatial partitioning with the ADMM solver. VastGaussian [60] and Hierarchy-GS [61] explore alternative partitioning strategies, each offering distinct architectural advantages. More recent developments include Octree-GS [12], which organizes Gaussian primitives in an octree structure to support adaptive multi-scale rendering, and CityGaussian [62], which incorporates level-of-detail techniques to optimize both training and rendering in urban-scale environments.

Despite these advances, two core limitations remain. First, rigid partitioning of space often breaks continuity of semantic structures, such as roads, facades or vegetation. Second, the lack of structural coordination and view-collaboration mechanisms limits the rendering fidelity required in large-scale scenarios. These challenges often lead to visual artifacts, such as ghosting, texture flickering, and inconsistent shading.

## III. METHOD

### A. Motivations & Overview

We propose a novel 3D Gaussian Splatting (3DGS) framework that integrates structure-aware and view-aware components to achieve fine-grained scene representation, enabling high-fidelity rendering, especially in large-scale environments. As illustrated in Fig. 2, our framework addresses two key limitations of existing approaches.

First, current 3DGS methods [8]–[10] either employ tri-plane structures or use context grid interpolation for spatial modeling. Both strategies have inherent limitations: Tri-plane representations often suffer from detail loss due to fixed-axis-aligned partitioning, while context interpolation lacks global spatial awareness. These issues result in reduced structural expressiveness and visual artifacts.

Second, traditional single-view optimization schemes [7] in 3DGS frameworks exhibit three major drawbacks: 1) susceptibility to overfitting to individual views, 2) discontinuities in regions with low view overlap, and 3) the accumulation of redundant Gaussians near camera paths.

To address the aforementioned limitations, we first introduce a Cross-Structure Collaboration Module (CSCM) that fuses multi-scale tri-plane features with context-aware grid features, enabling the simultaneous preservation of global spatial coherence and local geometric details. We then introduce a unified Cross-View Assisted Training Strategy (CVATS), which includes: 1) multi-view gradient alignment to reduce view-specific overfitting, 2) visibility-aware densification to improve coverage in sparsely observed areas, and 3) adaptive pruning based on geometric consistency to maintain point cloud integrity. Extensive experiments confirm the effectiveness of our proposed method, significantly improving rendering quality across diverse viewing conditions.

### B. Preliminary for 3D Gaussian Splatting

3D Gaussian Splatting [7] proposes a refined framework for scene representation, utilizing anisotropic 3D Gaussians as its core primitives. This method effectively integrates the differentiability inherent in volumetric representations with the computational efficiency of tile-based rasterization, achieving rapid rendering while preserving the capacity for gradient-based optimization.

3DGS begins by deriving a sparse point cloud from multi-view images using COLMAP, exemplified by tools such as Structure-from-Motion (SfM) techniques. Each Gaussian is parameterized by a mean position  $\mu \in \mathbb{R}^3$  and a covariance matrix  $\Sigma \in \mathbb{R}^{3 \times 3}$ , which jointly describe its anisotropic spatial distribution. The Gaussian function is mathematically defined as:

$$G(x) = \exp\left(-\frac{1}{2}(x - \mu)^\top \Sigma^{-1}(x - \mu)\right), \quad (1)$$

where  $x \in \mathbb{R}^3$  denotes a point in the 3D space. To ensure positive semi-definiteness of the covariance matrix, it is decomposed as:

$$\Sigma = RSS^\top R^\top, \quad (2)$$

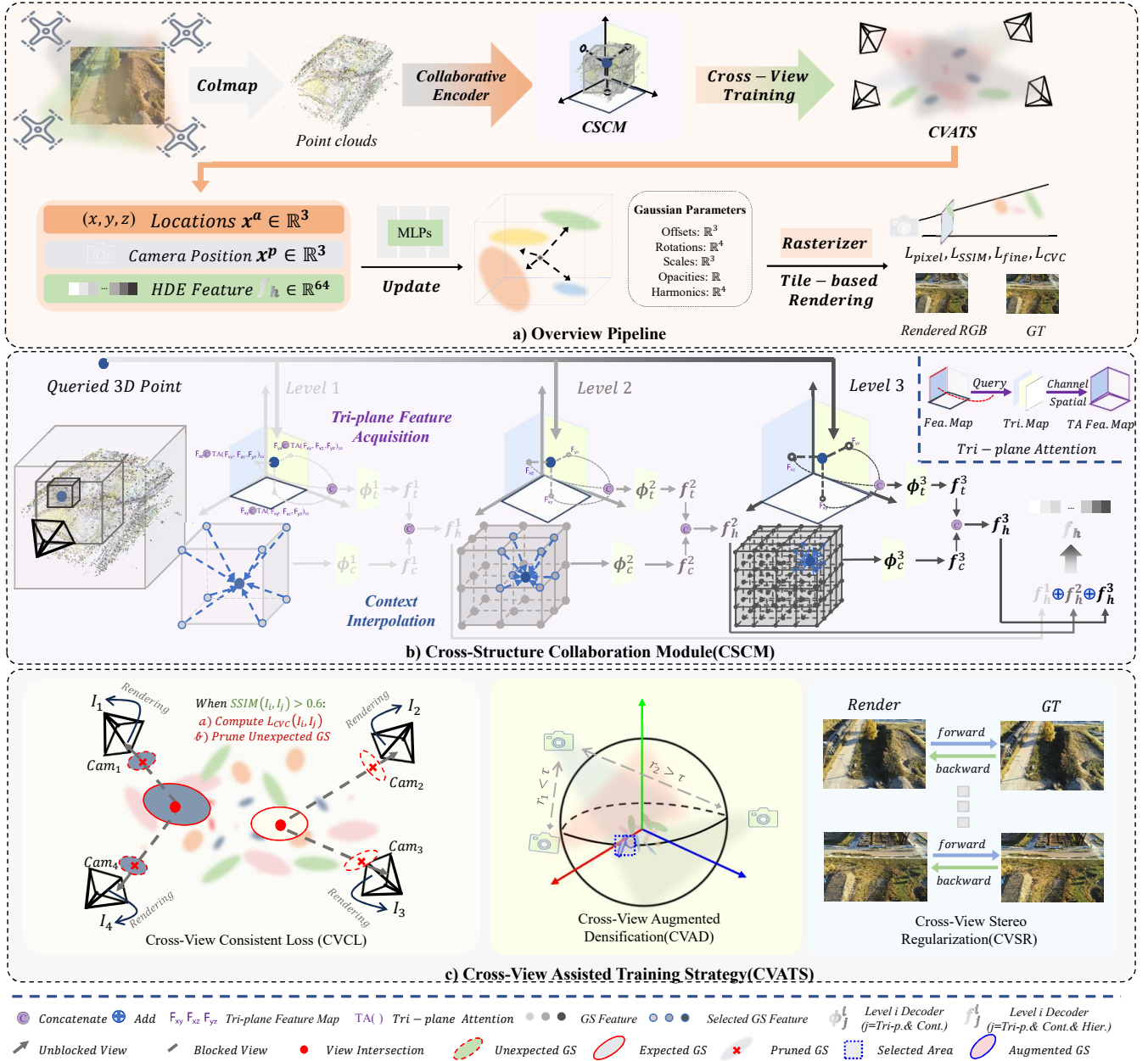


Fig. 2. **Overview.** We propose a Cross-Structure Collaboration Module (CSCM) that hierarchically integrates tri-planes with context grids, effectively preserving fine-grained details while maintaining consistent global geometry. Additionally, we introduce a Cross-View Assisted Training Strategy (CVATS) that enforces gradient consistency across overlapping cameras, effectively mitigating single-view overfitting in large-scale scenes. To further enhance generalization, we develop a structural-consistency-guided pruning mechanism, which iteratively removes over-specialized Gaussians, thereby preserving geometric integrity and ensuring robust performance across diverse viewpoints.

where  $S \in \mathbb{R}^{3 \times 3}$  is a diagonal matrix encoding scaling factors along principal axes, and  $R \in \mathbb{R}^{3 \times 3}$  is a rotation matrix aligning the Gaussian with the scene geometry.

For appearance modeling, each Gaussian is augmented with an opacity parameter  $\alpha \in [0, 1]$  to control transparency and spherical harmonic coefficients (SHs) to capture view-dependent color effects, represented as  $c$ . During rendering, the opacity  $\alpha$  modulates the Gaussian density  $G(x)$ , enabling precise regulation of translucency and supporting smooth blending of overlapping primitives.

The rendering process in 3DGS employs tile-based rasteri-

zation to optimize computational efficiency, circumventing the intensive demands of ray marching. Specifically, 3D Gaussians  $G(x)$  are projected onto the image plane, producing 2D Gaussian distributions  $G'(x')$ . A specialized tile-based rasterizer efficiently sorts and manages these projections by depth, applying  $\alpha$ -blending to composite their contributions into a final pixel color, expressed as:

$$C(x') = \sum_{i \in N} c_i \sigma_i \prod_{j=1}^{i-1} (1 - \sigma_j), \quad \sigma_i = \alpha_i G'_i(x'), \quad (3)$$

where  $x' \in \mathbb{R}^2$  represents a pixel coordinate, and  $N$  de-

notes the set of depth-ordered 2D Gaussians contributing to that pixel. The differentiable nature of this rasterization pipeline facilitates end-to-end optimization of all Gaussian attributes—position, covariance, opacity, and color—using gradient-based methods, ensuring robustness and flexibility across diverse scene types.

3DGS excels at balancing rendering speed with visual quality, offering a compelling alternative to traditional volumetric rendering approaches. By harnessing hardware acceleration and avoiding per-pixel ray tracing, 3DGS provides an efficient pipeline well-suited for real-time applications while retaining the adaptability required for high-fidelity scene reconstruction.

### C. Cross-Structure Collaboration Module

The tri-plane and context grid structures are two powerful representations for encoding 3D point cloud features. Both methods utilize interpolation to extract features at any arbitrary point within the 3D space. The former achieves this by applying interpolation across the entire point cloud feature map, while the latter accomplishes it through local resolution grids. However, both of these structures have their respective limitations: *the tri-plane structure emphasizes global features while neglecting the local relationships between points in the point cloud, and the context grid structure focuses on interpolation within resolution grids, making it challenging to capture the spatial correlations of the entire point cloud.*

Therefore, we propose the Cross-Structure Collaboration Module (CSCM), which integrates the global perception of the tri-plane structure with the local sensitivity of the context grid structure. This approach facilitates more accurate feature extraction for each Gaussian point within the overall point cloud, significantly improving the quality of rendering details in subsequent novel view synthesis. Inspired by Feature Pyramid Networks (FPN) [63], we divide the overall training process into three levels. During training, features are progressively compensated from coarse to fine, aiming to reduce feature misalignment caused by the size of the tri-plane feature map and grid resolution. Specifically, the CSCM consists of three components: **tri-plane feature acquisition**, **context interpolation**, and **cross-structure hierarchical compensation**.

**Tri-plane Feature Acquisition.** Tri-Plane is a static 3D instance of the  $k$ -planes factorization [64], which represents the 3D space using three  $m$ -channel feature plane maps  $\mathbf{F} \in \mathbb{R}^{w \times h \times m}$ , each corresponding to one of the axis-aligned planes:  $xy$ ,  $xz$ , and  $yz$ , with spatial resolution  $w \times h$ . To obtain fine-grained tri-plane features for a queried 3D point  $\mathbf{p}$ , we first apply a tri-plane attention module to generate attention-enhanced tri-plane features  $\mathbf{F}^{TA}$ . This module captures relative features across all three planes from the global tri-plane context, thereby enhancing the global perception capability compared to traditional tri-plane representations that focus solely on individual planes. The formulation is as follows:

$$\mathbf{F}_i^{TA} = \text{TA}(\mathbf{F}_i), \quad (4)$$

$$\text{TA}(\mathbf{F}_i) = \rho_i(\text{SA}(\text{CA}(\|\_{j \in \{xy, xz, yz\}}(\mathbf{F}_j))), \quad (5)$$

where  $i$  denotes the axis-aligned planes:  $xy$ ,  $xz$ , and  $yz$ , and  $\text{TA}(\cdot)$  represents the tri-plane attention operation. The operator

$\|\_{j \in \{xy, xz, yz\}}(\cdot)$  indicates concatenating feature planes along the channel dimension in the order of  $xy$ ,  $xz$ , and  $yz$ .  $\text{SA}(\cdot)$  and  $\text{CA}(\cdot)$  denote the spatial attention and channel attention operations [65] applied to the feature maps, respectively.  $\rho_i(\cdot)$  corresponds to the operation of extracting the tri-plane attention feature map for the dimension indexed by  $i$  from the previously concatenated feature maps.

We then project the given 3D point  $\mathbf{p}$  onto these planes and interpolate the features on the corresponding grids. The interpolated features are then concatenated to form the feature representation for this point. Finally, the decoder  $\phi_t$  is used to obtain the tri-plane feature  $f_t$  for the point:

$$f_t = \phi_t(\|\_{i \in \{xy, xz, yz\}}(\psi(\mathbf{F}_i, \pi_i(\mathbf{p})), \psi(\mathbf{F}_i^{TA}, \pi_i(\mathbf{p}))), \quad (6)$$

where  $\pi_i(\cdot)$  is the projection function, and  $\psi(\cdot)$  denotes bilinear interpolation on the feature map.  $\phi_t(\cdot)$  represents the tri-plane feature decoder. We first concatenate the interpolated original features from both the original and attention-enhanced feature maps of the same orientation. Then, the features from different tri-plane orientations are sequentially concatenated along the channel dimension. Finally, the concatenated features are passed through the decoder to obtain the tri-plane feature  $f_t$ .

**Context Interpolation.** In addition to leveraging tri-plane features for global scene perception, we aim to uncover the local intrinsic relationships between the 3D Gaussians that construct the scene. To achieve this, we employ grid-based structures to obtain contextual interpolation features for each Gaussian point, which are typically compact, well-organized, and capable of establishing spatial connections among the Gaussians.

To obtain the contextual interpolation information for the current query Gaussian point  $p$ , we first create a grid structure for the current point cloud based on the given resolution  $\alpha$ . As shown in Fig. 2(b), the vertices of the cube with blue contours represent the context Gaussians for interpolation of the query Gaussian. Then, based on the distance between the query Gaussian point  $p$  and the vertices of the corresponding grid, we use the features  $f_g$  of the vertex Gaussians to perform a weighted aggregation. Finally, the decoder  $\phi_c$  is used to decode and obtain the contextual feature  $f_c$  for the current point:

$$f_c = \phi_c \left( \frac{\sum_{v \in G} w_v \times f_g}{\sum_{v \in G} w_v} \right), \quad (7)$$

$$w_v = \prod_{\text{dim} \in \{x, y, z\}} (1 - \{\mathbf{p}_{\text{dim}} - v_{\text{dim}}\}), \quad (8)$$

$$f_g = [f_p, p, O, s], \quad (9)$$

where  $G$  is the resolution grid that the query point  $\mathbf{p}$  falls on, and  $v$  represents the vertices of  $G$ . The notation  $\{\cdot\}$  is used to compute the normalized absolute distance between the coordinates of two points along each axis, while  $[\cdot]$  denotes the concatenation operation.  $f_p$  refers to the inherent features of the query point,  $O$  is the offset of the neural Gaussian center associated with the query point, and  $s$  denotes the scales of these Gaussians.

**Cross-Structure Hierarchical Compensation.** Once we have obtained the global features  $f_t$  of the query point  $p$  from the tri-plane structure and the local features  $f_c$  from the contextual grid interpolation, we propose a cross-structure compensation mechanism to fully leverage the advantages of both types of features. This mechanism results in the refined feature  $f_h$ , which captures both global and local point cloud relationships:

$$f_h = [f_t, f_c]. \quad (10)$$

Additionally, considering that the refinement of scene representation by both structural features is limited to some extent by the resolution of the feature maps and the grid resolution, we introduce a hierarchical compensation mechanism based on the cross-structure refined features. We divide the overall training process into three levels, progressively increasing the resolution of the tri-plane feature maps and utilizing finer contextual grids as the training progresses. The refined features  $f_h$  from each level are then merged:

$$f_h = \sum_{i \in L} f_h^i. \quad (11)$$

Here,  $L$  denotes the number of levels, and  $f_h^i$  represents the cross-structure refined features at the  $i$ -th level. Thus,  $f_h$  provides the ability to capture fine scene details for subsequent rendering.

#### D. Cross-View Assisted Training Strategy

Although we have previously derived cross-structure collaborative features that effectively capture the Gaussian point distribution, the inherent reliance on single-view image-based optimization in the original 3DGS method exacerbates the overfitting of Gaussians to the training viewpoint. As illustrated in the left side of Fig. 2 (c), the Gaussian ellipsoids compensate for the current training viewpoint by being distributed extremely close to the camera position. However, they do not lie in positions that are realistically generalizable to new viewpoints, leading to significantly better rendering quality for the training viewpoint compared to the test viewpoint, thus causing overfitting. Moreover, in large-scale scenes, the overfitting issue becomes more pronounced due to the limited overlap between images from different viewpoints.

To address this issue, we propose a Cross-View Assisted Training Strategy (CVATS). Specifically, we first introduce a **cross-view stereo regularization** method that leverages multiple views for collaborative optimization. Additionally, we propose **cross-view augmented densification** to improve point distribution by incorporating information from spatially distant views, which is particularly advantageous in large-scale scenes. Finally, a **cross-view consistent loss** strategy is employed to enforce coherence between adjacent viewpoints and mitigate overfitting of Gaussians.

**Cross-View Stereo Regularization.** Unlike the original single-view iterative training, we introduce a cross-view stereo approach that optimizes 3D Gaussians with multi-view supervision. In each iteration, we sample  $M$  pairs of images and camera parameters, ensuring they are distinct from one

another. Our multi-view regulated learning, which integrates gradients in a single iteration, is formulated as:

$$\frac{\partial \mathcal{L}}{\partial \{G\}} = \frac{\partial \mathcal{L}(G_1, E_1, K_1)}{\partial G_1} + \dots + \frac{\partial \mathcal{L}(G_M, E_M, K_M)}{\partial G_M}, \quad (12)$$

where  $\mathcal{L}$  represents the loss at the current iteration. Let  $G = \{G_1, G_2, \dots, G_M\}$  denote the set of 3D Gaussians, with each  $G_M$  being affected by large gradients from each view during multi-view training. The extrinsic and intrinsic parameters of the camera are denoted by  $E_M$  and  $K_M$ , respectively.

The key distinction from the original 3DGS loss is that our approach incorporates a multi-view gradient constraint to optimize the 3D Gaussians. This allows each Gaussian kernel  $g_i$  to be adjusted based on multi-view information, effectively reducing overfitting to individual views. Additionally, the multi-view constraint helps the 3D Gaussians learn view-dependent features, such as reflections (illustrated in the left part of Fig. 2(c)), enabling improved performance in novel view synthesis for reflective scenes.

**Cross-View Augmented Densification.** When optimizing across multiple viewpoints, particularly in large-scale scenes, selecting views that are too far apart is common. This results in limited overlap between perspectives, which increases the risk of overfitting Gaussian ellipsoids. To address this, we first normalize the camera translations of sampled views to fit within a unit sphere, making our method adaptable to various scenes. We then compute the relative translation distances  $\{r_i \mid i = 1, 2, \dots, M\}$  between the cameras. Our multi-view augmented densification employs a self-adaptive threshold  $\hat{\beta}$ , which is formulated as:

$$\hat{\beta} = \frac{\beta}{2} H\left(\frac{r_i}{\tau} - 1\right) + \beta \left(1 - H\left(\frac{r_i}{\tau} - 1\right)\right), \quad (13)$$

where  $H(\cdot)$  is the Heaviside function, returning 1 if the input is greater than or equal to 0.  $\beta$  is the threshold for the original 3DGS densification, and  $\tau$  is a predefined hyperparameter.

This approach ensures that when discrepancies between views increase, the extent of 3D Gaussian densification is also enhanced.

**Cross-View Consistent Loss.** To enhance the continuity of scene structures and reduce overfitting of Gaussians, we first select adjacent views from the  $M$  viewpoints, using the Structural Similarity Index Measure (SSIM) between images as a selection criterion, with the condition that the SSIM value is greater than 0.6. Next, we compute the Cross-view Consistent Loss  $L_{CVC}$  between two images and obtain a mask  $M_f$  to remove overfitted Gaussians:

$$L_{CVC} = SSIM(I_i^{gt}, I_j^{gt}) * L_1(I_i^{gt} - I_i, I_j^{gt} - I_j), \quad (14)$$

$$M_f(\mathbf{p}) = \begin{cases} 1, & \text{if } \alpha(\mathbf{p}) = True \\ 0, & \text{otherwise} \end{cases} \quad (15)$$

$$\alpha(\mathbf{p}) = d_I(\mathbf{p}) < 0.01 \wedge (d_C(\mathbf{p}) < 0.5 \vee d_O(\mathbf{p}) > 3\sigma). \quad (16)$$

Here,  $M_f(\mathbf{p}) = 1$  indicates that the Gaussian point  $\mathbf{p}$  is considered an overfitted Gaussian and should be pruned.  $d_I$  represents the distance from the Gaussian point to the camera's viewpoint ray, and when  $d_I < 0.01$ , we assume that the point is intersected by the viewpoint ray.  $d_C$  is the distance

TABLE I  
 QUANTITATIVE COMPARISON ON MILL-19 AND MATRIXCITY DATASETS. THE ‘-’ SYMBOL REPRESENTS MEGA-NeRF [66] AND SWITCH-NeRF [67] WERE NOT EVALUATED ON MATRIXCITY. THE BEST, SECOND-BEST, AND THIRD-BEST RESULTS ARE MARKED IN RED, ORANGE, AND YELLOW, RESPECTIVELY.

Metrics	MatrixCity			Rubble			Building		
	SSIM↑	PSNR↑	LPIPS↓	SSIM↑	PSNR↑	LPIPS↓	SSIM↑	PSNR↑	LPIPS↓
Mega-NeRF [CVPR22] [66]	-	-	-	0.553	24.06	0.516	0.547	20.93	0.504
Switch-NeRF [ICLR22] [67]	-	-	-	0.562	24.31	0.496	0.579	21.54	0.474
3DGS [ToG23] [7]	0.737	23.79	0.384	0.746	24.30	0.324	0.676	20.11	0.372
GaMeS [arXiv24] [68]	0.773	24.64	0.367	0.767	24.64	0.311	0.698	20.97	0.329
Compact3DGS [CVPR24] [69]	0.795	26.03	0.370	0.719	23.01	0.373	0.645	20.00	0.425
Scaffold-GS [CVPR24] [70]	0.842	27.25	0.290	0.736	23.71	0.346	0.711	21.55	0.328
Pixel-GS [ECCV24] [71]	0.814	25.60	0.324	0.771	24.67	0.308	0.700	21.00	0.352
Ours	0.855	28.05	0.249	0.794	26.90	0.280	0.759	23.03	0.270

from the Gaussian point to the camera position, and  $d_O$  denotes the distance from the Gaussian point to the average position of the point cloud. If  $d_C < 0.5$  or  $d_O > 3\sigma$  where  $\sigma$  is the point cloud’s variance, we regard the Gaussian as a visual overfitting point in the training view that neglects scene structure consistency, and it will be pruned. In this way, we optimize the distribution of Gaussians during training, effectively reducing the risk of overfitting.

#### E. Update Gaussian Attributes & Rasterization

To fully leverage the features previously acquired, we employ the method of neural Gaussians [70] obtained earlier.

We integrate Gaussian positions, camera poses, and hierarchical features through multiple MLPs to update Gaussian attributes such as position  $\mu \in \mathbb{R}^3$ , opacity  $\alpha \in \mathbb{R}$ , quaternion  $q \in \mathbb{R}^4$ , scaling  $s \in \mathbb{R}^3$ , and color  $c \in \mathbb{R}^3$ . For each visible anchor,  $k$  Gaussians are generated and their respective attributes are computed. The position of the Gaussian primitives corresponding to an anchor at  $x^a$  is derived as follows:

$$\{\mu_0, \dots, \mu_{k-1}\} = x^a + \{O_0, \dots, O_{k-1}\} \cdot l^a, \quad (17)$$

where  $\{O_0, O_1, \dots, O_{k-1}\} \in \mathbb{R}^{k \times 3}$  are learnable offsets, and  $l^a$  is a learnable scaling factor. The attributes of the Gaussians are obtained using MLPs:

$$\{\mathcal{A}_0, \dots, \mathcal{A}_{k-1}\} = \text{MLPs}([x^a, x^p, f_h]), \quad (18)$$

where  $\mathcal{A}_i$  represents the parameters of the  $k$  Gaussian primitives for each anchor, and  $[\cdot]$  denotes the concatenation operation.

After determining the parameters for each Gaussian, we use rasterization methods as outlined in 3DGS [7] to generate rendered images from the respective viewpoints. The network parameters are then optimized according to the loss functions detailed below.

## IV. LOSS FUNCTION

In summary, our loss function consists of three components: 1) rendering pixel loss  $L_{\text{pixel}}$ , 2) Structural Similarity Index Measure (SSIM) loss  $L_{\text{SSIM}}$  [72], 3) fine-grained Gaussian regularization loss  $L_{\text{fine}}$ , 4) cross-view consistent loss  $L_{\text{CVC}}$ .

#### A. Rendering Loss

The rendering loss measures pixel-level color differences between the training and rendered images using the  $L_1$  norm. Specifically, the  $L_{\text{pixel}}$  is defined as:

$$L_{\text{pixel}} = \frac{1}{N} \sum_{i=1}^N |I_i^{\text{gt}} - I_i|, \quad (19)$$

where  $I_{\text{rendered}}$  denotes the rendered image,  $I_{\text{gt}}$  represents the ground truth, and  $N$  is the total number of pixels in the image.

#### B. Structural Similarity Index Measure Loss

SSIM is employed to assess the structural similarity between two images, evaluating differences in brightness, contrast, and structure. The loss function is formulated as:

$$L_{\text{SSIM}} = 1 - \text{SSIM}(I_i^{\text{gt}}, I_i), \quad (20)$$

where the  $\text{SSIM}(\cdot)$  function computes the Structural Similarity Index between the rendered image and the ground truth.

#### C. Fine-Grained Gaussian Regularization Loss

To improve the ability of Gaussian primitives to capture finer scene details, we introduce a regularization loss that minimizes the volume of Gaussian ellipsoids. The loss is defined as follows:

$$L_{\text{fine}} = \sum_{i=1}^{N_g} \prod (s_i), \quad (21)$$

where  $N_g$  represents the number of neural Gaussians in the scene, and  $\prod(\cdot)$  indicates the product of the elements in a vector. In this case, it applies to the scale values  $s_i$  of each Gaussian.

#### D. Overall Loss

The total loss is a weighted sum of the individual loss terms:

$$\mathcal{L} = (1 - \lambda_1)L_{\text{pixel}} + \lambda_1 L_{\text{SSIM}} + \lambda_2 L_{\text{fine}} + \lambda_3 L_{\text{CVC}} \quad (22)$$

where  $\lambda_1$ ,  $\lambda_2$  and  $\lambda_3$  are the weights to control the relative importance of each loss term. In our implementation, we empirically set the weights as:  $\lambda_1 = 0.2$ ,  $\lambda_2 = 0.01$  and  $\lambda_3 = 0.05$ .

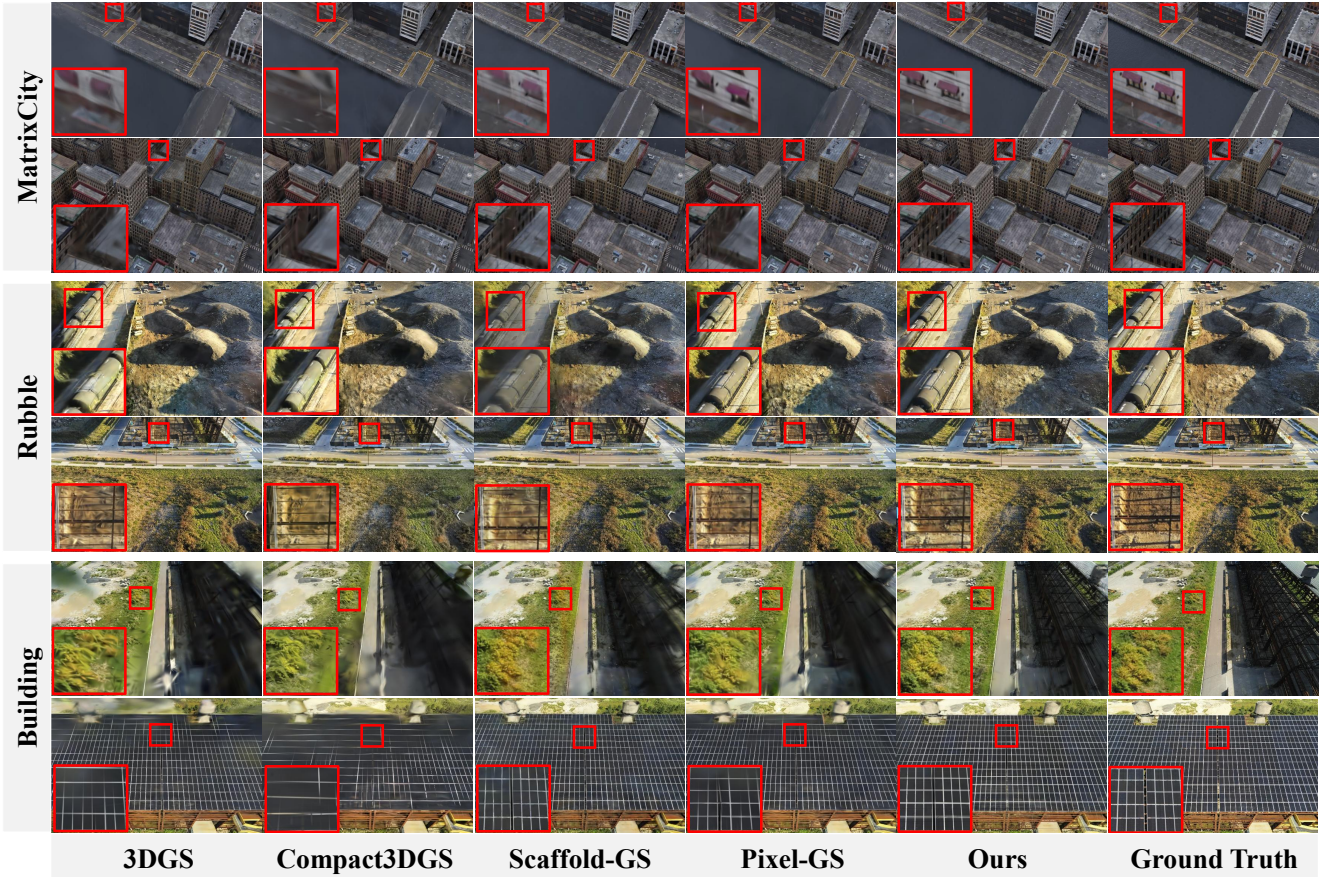


Fig. 3. Qualitative comparison of our method with existing advanced techniques on the MatrixCity and Mill-19 datasets. Red boxes are used to highlight visual differences. As illustrated, in the building scene, our method achieves high-fidelity fine-grained reconstruction of complex textures, such as the exterior of solar panels, surpassing other methods. Please *zoom in* for more detailed visual results.

## V. EXPERIMENTS

### A. Datasets

We assess the performance of our method by comparing it with state-of-the-art approaches on 13 outdoor scenes of diverse scales, which include eight scenes from four publicly available datasets and five scenes collected independently.

**Public Scenes.** We perform evaluations on eight scenes, which include the Rubble and Building from the Mill-19 dataset [66], MatrixCity from the city-scale MatrixCity-Aerial dataset [73], and Train and Truck from the Tanks & Temples dataset [74]. Additionally, we select three particularly challenging aerial scenes from areas 1, 4, and 5 of the WHU dataset [75] to assess the performance of various methods.

**Self-collected Scenes.** To further evaluate the performance of our method in campus environments and plateau regions with large coverage areas and rich details, we collect the SCUT Campus Aerial (SCUT-CA) scenes, which consist of three scenes featuring teaching, office, and history museum buildings. Specifically, we use the DJI Matrice 300 RTK to capture images from approximately 100 meters above three distinct scenes at the Wushan Campus of South China University of Technology, with 125, 197, and 273 images, respectively, totaling 595 images. Each image has a resolution of

4082×2148. To maintain consistency with the 3DGS [7] input, we downsample the images to a resolution of 1600×841.

We also collect scenes from plateau regions, which include two scenes characterized by vast distribution, along with diverse geographical features. Specifically, we use the DJI Matrice 300 to capture images at an altitude of approximately 100 meters in the plateau region (Linzhi, Tibet), obtaining 203 and 170 images, respectively, for a total of 373 images. Each image has a resolution of 6222×4148, and we downsample these images to a resolution of 1600×841 as well. Camera parameters are estimated using widely adopted techniques such as COLMAP [76].

### B. Evaluation Metrics

Following previous methods [7], [66], we primarily evaluate the quality of the rendered images using three metrics: PSNR, SSIM [72], and the VGG implementation of LPIPS [77].

### C. Implementation Details

Our experiments are conducted on an NVIDIA 3090 GPU using PyTorch, with each scene trained for 30,000 iterations. In the cross-structure collaboration module, we progressively activate the process of acquiring cross-structure features at three granularities—coarse to fine—during training iterations

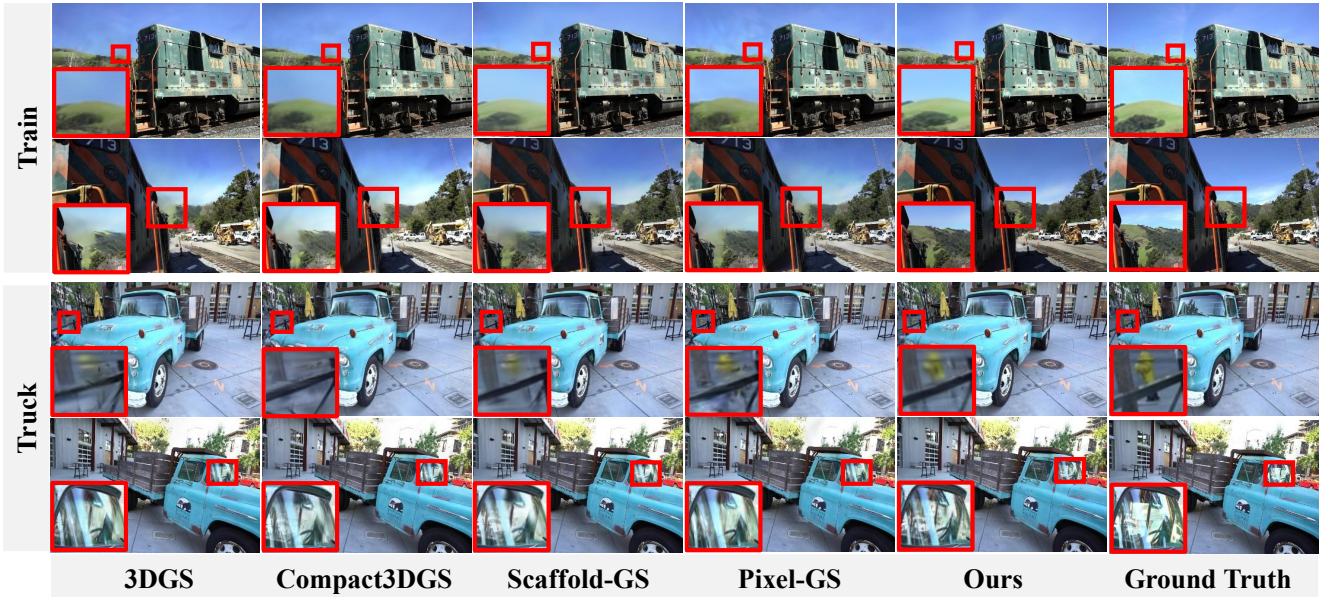


Fig. 4. Novel view synthesis results on the Tanks & Temples dataset. Our method, leveraging structure-view assisted learning, achieves superior detail in challenging scenarios. This is evidenced by the sharper reconstruction of distant mountain edges in the train scene and the comprehensive modeling of glass reflection details in the truck scene, highlighting the efficacy of our approach.

1, 12,000, and 21,000, respectively. At each level, the pixel resolution of the tri-plane feature maps is doubled compared to the previous level, while the density of the context grid is also increased by a factor of two. To optimize both computational efficiency and rendering performance, we apply the tri-plane spatial attention mechanism for enhancement solely at the first level’s tri-plane feature maps. In the cross-view assisted training strategy, we sample four pairs of images and camera parameters in each training iteration. Additionally, we set the hyperparameter  $\tau$  to 1.0 to maximize rendering performance. In our experiments, the MLPs used to update Gaussian attributes, as well as those in the cross-structure collaboration module, both consist of two layers, with the latter incorporating an additional batch normalization operation. All parameters related to Gaussian optimization and the densification process are set according to the original configurations from previous methods [70].

#### D. Result Analysis

1) *Result on Mill-19 and MatrixCity dataset:* We rigorously evaluate our method through comprehensive quantitative and qualitative analyses. As shown in Table. I, our approach achieves state-of-the-art performance across three scenarios: MatrixCity, Rubble and Building. In the Building scene, our approach achieves substantial gains over Scaffold-GS, with margins of +0.048 (SSIM), +1.48 (PSNR), and +0.058 (LPIPS), underscoring its superior rendering quality. We attribute this superiority to our collaborative framework’s enhanced adaptability to spatially structured scenes - compared to Scaffold-GS’s hash grid encoding, our architecture models geometric priors more effectively. Notably, Pixel-GS exhibits marked performance degradation in this scenario, suggesting that pixel-optimized point cloud processing struggles with

large-scale environments containing complex spatial structures. Fig. 3 presents visual comparisons between our method and existing 3DGS baselines. The experimental results show that our approach consistently preserves high-fidelity detail reconstruction while effectively mitigating artifacts common in other methods. Particularly in the Building scene, our method achieves more accurate reconstruction of fine structural details such as solar panel grid patterns, demonstrating clear advantages over competing approaches.

TABLE II  
QUANTITATIVE COMPARISON ON TANKS & TEMPLES DATASET. THE BEST, SECOND-BEST, AND THIRD-BEST RESULTS ARE MARKED IN RED, ORANGE, AND YELLOW, RESPECTIVELY.

Metrics	Train			Truck		
	SSIM $\uparrow$	PSNR $\uparrow$	LPIPS $\downarrow$	SSIM $\uparrow$	PSNR $\uparrow$	LPIPS $\downarrow$
Mip-NerF360 [CVPR22] [78]	0.660	19.52	0.354	0.857	24.91	0.159
iNPG [T6G22] [79]	0.666	20.17	0.386	0.779	23.26	0.274
Plenoxels [CVPR22] [80]	0.663	18.93	0.422	0.774	23.22	0.335
3DGS [T6G23] [7]	0.815	22.07	0.208	0.882	25.46	0.147
GaMeS [arXiv24] [68]	0.816	22.11	0.205	0.877	25.24	0.151
Compact3DGS [CVPR24] [69]	0.792	21.56	0.240	0.871	25.07	0.163
Scaffold-GS [CVPR24] [70]	0.816	22.32	0.213	0.886	25.83	0.141
Pixel-GS [ECCV24] [71]	0.813	22.01	0.188	0.872	25.03	0.131
Ours	0.840	23.76	0.158	0.881	26.09	0.126

2) *Result on Tanks & Temples dataset:* We present the quantitative results on Tanks and Temples in Table. II. Our method demonstrates consistent superiority over other competitive approaches across all metrics on the ‘train’ scene. Specifically, compared to Scaffold-GS, our approach achieves significant improvements of 0.024 in SSIM, 1.44 in PSNR, and 0.055 in LPIPS. As visually confirmed in Fig. 4, our method effectively separates the background sky from distant mountains in the rendered imagery. For the ‘truck’ scene, our method exhibits superior performance in both PSNR and LPIPS metrics compared to other approaches. While it shows a marginal 0.005 deficit in SSIM relative to Scaffold-GS,

TABLE III  
 QUANTITATIVE COMPARISON ON SCUT\_CA OUTDOOR SCENES. THE BEST, SECOND-BEST, AND THIRD-BEST RESULTS ARE MARKED IN RED, ORANGE, AND YELLOW, RESPECTIVELY.

Metrics	Tower Two			School History Museum			EI School		
	SSIM $\uparrow$	PSNR $\uparrow$	LPIPS $\downarrow$	SSIM $\uparrow$	PSNR $\uparrow$	LPIPS $\downarrow$	SSIM $\uparrow$	PSNR $\uparrow$	LPIPS $\downarrow$
3DGS [ToG23] [7]	0.887	29.87	0.143	0.849	28.54	0.189	0.882	29.12	0.132
GaMeS [arXiv24] [68]	0.891	29.99	0.140	0.861	28.83	0.182	0.889	29.36	0.120
Compact3DGS [CVPR24] [69]	0.873	29.03	0.164	0.844	27.96	0.211	0.863	27.97	0.160
Scaffold-GS [CVPR24] [70]	0.880	29.49	0.155	0.854	28.44	0.197	0.873	28.67	0.147
Pixel-GS [ECCV24] [71]	0.915	30.81	0.097	0.882	29.34	0.142	0.909	29.77	0.092
Ours	0.916	31.25	0.100	0.887	29.87	0.130	0.912	30.53	0.090

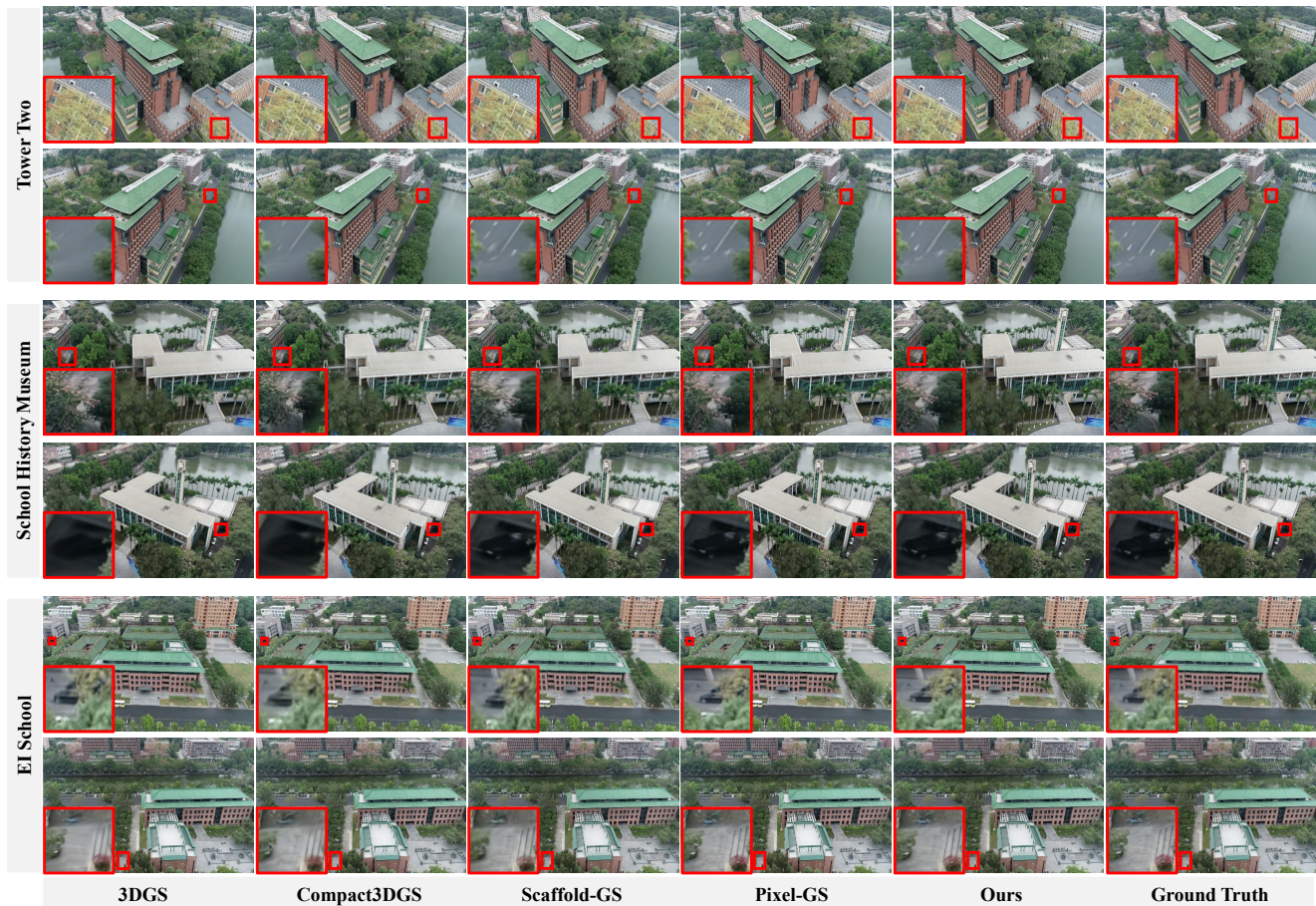


Fig. 5. Visualization results on our custom SCUT\_CA dataset. Highlighted regions (e.g., red boxes) reveal that our method renders significantly finer details and more realistic textures for elements such as leaves, lane markings, and distant objects, underscoring its superiority over competing approaches.

our method produces visually superior results. Specifically, it better reconstructs fire hydrant contours and significantly reduces artifacts in the truck’s window regions.

3) *Result on SCUT-CA scenes*: We further evaluate our method’s performance on our custom SCUT-CA dataset. As shown in Table. III, our approach demonstrates superior performance across all evaluation metrics in both the School History Museum and EI School scenes when compared to other baseline methods. While exhibiting a marginal 0.003 deficit in LPIPS when compared to Pixel-GS, our method shows significant advantages in both SSIM and PSNR metrics. Notably, Scaffold-GS exhibits substantial performance degradation on our custom dataset in comparison to public scene datasets, whereas our method maintains consistently ro-

bust performance. This enhanced robustness can be attributed to our structure-view collaborative learning mechanism. The comparative results in Fig. 5 reveal that the original 3DGS fails to reconstruct the zebra crossing details in the scene, while our method not only accurately recovers these fine details but also significantly reduces rendering artifacts. Furthermore, we observe that in the School History Museum scene, both 3DGS and Compact3DGS fail to effectively render vehicle wheels.

4) *Result on WHU dataset and Plateau Region scenes*: We systematically evaluate our method on both the WHU dataset and plateau scenes, with quantitative and qualitative results presented in Table. IV and Fig. 6, respectively. The WHU dataset is characterized by significant image blurring, while the plateau scenes exhibit distinct planar features. As

TABLE IV  
 QUANTITATIVE COMPARISON ON WHU DATASET AND PLATEAU REGION SCENES. THE BEST, SECOND-BEST, AND THIRD-BEST RESULTS ARE MARKED IN RED, ORANGE, AND YELLOW, RESPECTIVELY.

Metrics	WHU									Plateau Region					
	Area1			Area4			Area5			Scene1			Scene2		
	SSIM $\uparrow$	PSNR $\uparrow$	LPIPS $\downarrow$	SSIM $\uparrow$	PSNR $\uparrow$	LPIPS $\downarrow$	SSIM $\uparrow$	PSNR $\uparrow$	LPIPS $\downarrow$	SSIM $\uparrow$	PSNR $\uparrow$	LPIPS $\downarrow$	SSIM $\uparrow$	PSNR $\uparrow$	LPIPS $\downarrow$
3DGS [10623] [7]	0.887	30.84	0.216	0.901	28.87	0.200	0.799	26.04	0.329	0.723	28.46	0.334	0.745	29.62	0.369
GaMeS [arXiv24] [68]	0.902	31.28	0.207	0.892	28.34	0.203	0.812	26.48	0.311	0.783	29.24	0.308	0.759	29.79	0.363
Compact3DGS [CVPR24] [69]	0.922	32.69	0.217	0.946	33.79	0.147	0.865	28.37	0.273	0.721	28.32	0.355	0.721	29.78	0.400
Scaffold-GS [CVPR24] [70]	0.978	38.90	0.068	0.980	38.86	0.063	0.964	34.70	0.089	0.787	29.66	0.308	0.737	30.06	0.393
Pixel-GS [ECCV24] [71]	0.814	23.51	0.343	0.806	21.07	0.321	0.631	17.61	0.474	0.663	28.20	0.486	0.743	30.42	0.440
Ours	0.988	42.27	0.034	0.987	41.20	0.040	0.975	37.13	0.058	0.734	29.03	0.332	0.769	30.68	0.359

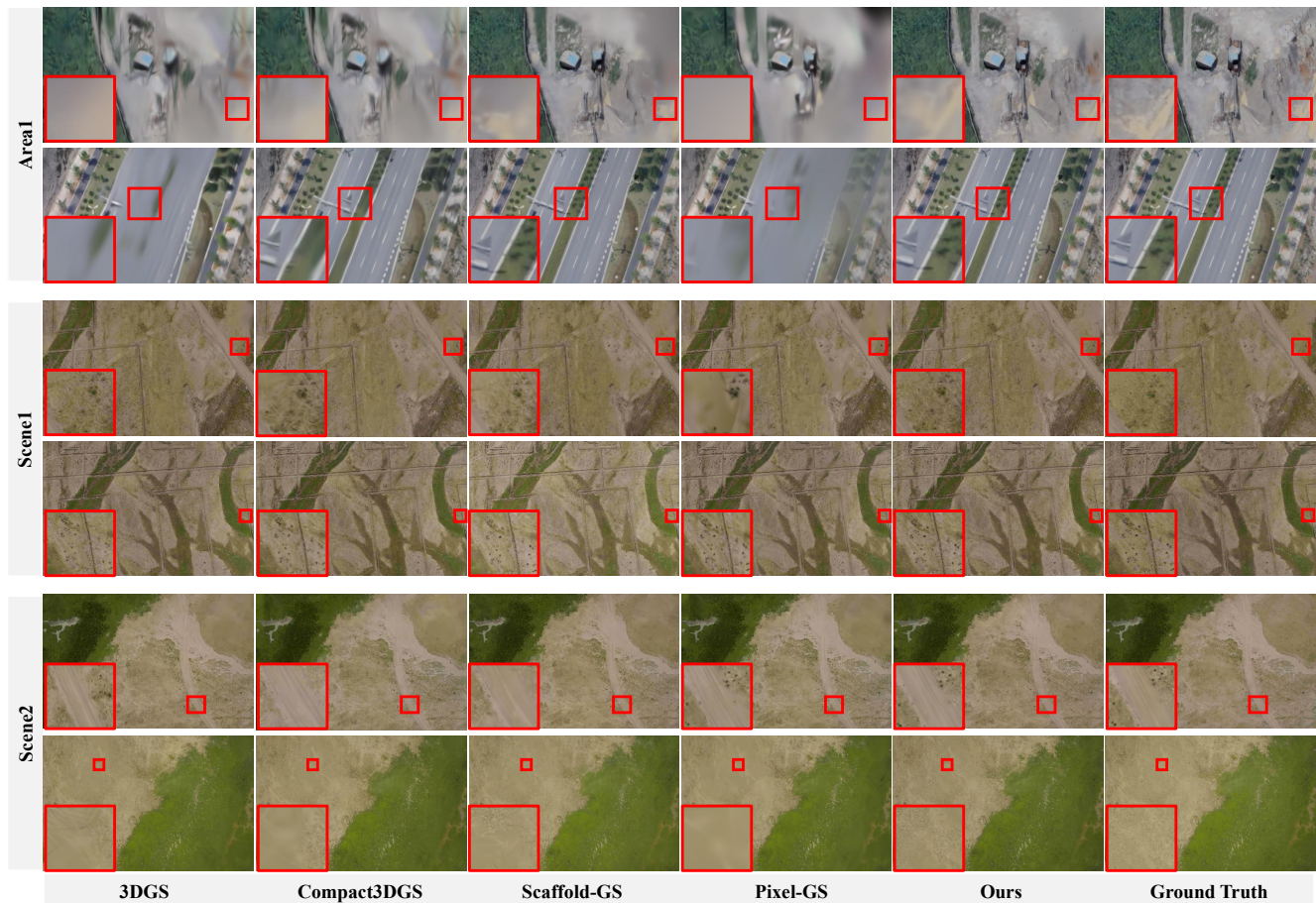


Fig. 6. Results on the WHU dataset and plateau region scenes, our method achieves highly realistic modeling of broad scene structures and precise capture of fine surface details. For instance, 'area' showcases more authentic land and road structures. Simultaneously, our method accurately delineates subtle features like the distribution of vegetation on plateaus and the complex surface textures of sandy terrains, demonstrating superior structural awareness and detail retrieval.

demonstrated in Table. IV, our method maintains superior performance metrics even under challenging low-quality blurry conditions. Notably, in the plateau scene evaluation, our method achieves optimal results in Scene 2 but exhibits marginally degraded performance in Scene 1. Through rigorous analysis, we attribute the performance gap to non-uniform sampling during data acquisition in Scene 1, where the drone captured images at varying altitudes during its ascent. This inconsistency in viewpoint distribution disrupts the cross-view collaborative learning mechanism that our proposed Cross-View Assisted Training Strategy relies on, ultimately leading to degraded model performance. Furthermore, our experiments reveal that mesh-based methods (e.g., GaMeS) demonstrate

particularly strong performance in planar regions, owing to their inherent advantages in geometric representation using mesh structures. Visual comparisons in Fig. 6 show that our method does not have artifacts, and contains more details with much higher accuracy than other methods.

#### E. Ablation Study

1) *Effectiveness of Cross-Structure Collaboration Module:* We conduct an ablation study on our proposed cross-structure collaboration module under three configurations: (1) using only context grid encoding, (2) using only tri-plane feature encoding, and (3) combining both encodings. Additionally, we compare two feature fusion strategies: direct concatenation and

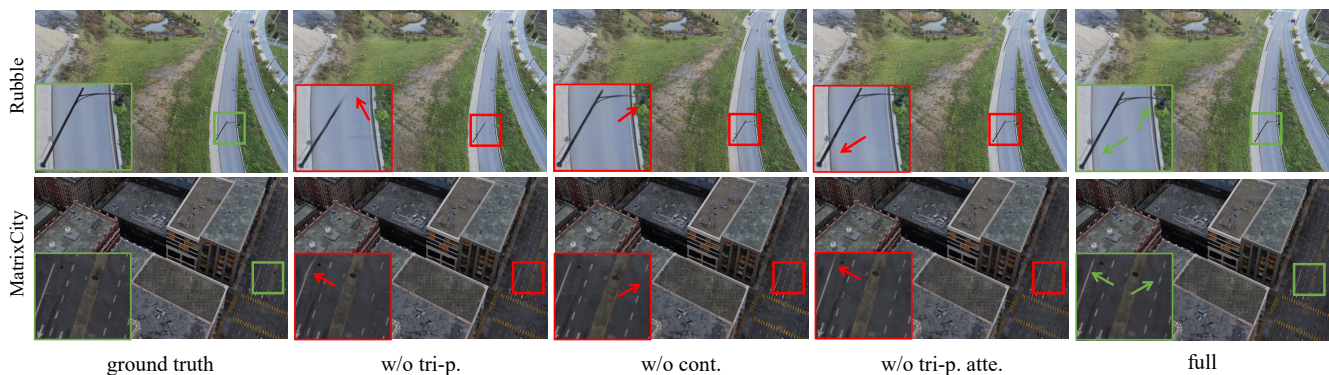


Fig. 7. Impact of the cross-structure collaborated module, demonstrated via ablation. Red and green boxes demarcate visual distinctions. By fusing attention-enhanced tri-plane features with context grid features, the module yields demonstrably more refined rendering and improved structural integrity. This stems from its enhanced ability to perceive both overarching point cloud architecture and fine-grained local details. Please *zoom in* to view detailed results.

attention-based fusion. As shown in Table. V, our experiments demonstrate that (1) fusing both encoding structures significantly improves performance, and (2) employing a lightweight attention mechanism further enhances the results. Qualitative results in Fig. 7 show that our cross-structure collaboration module generates rendered results with sharper line details.

TABLE V  
ABLATION STUDY ON CROSS-STRUCTURE COLLABORATED MODULE.

method	SSIM $\uparrow$	PSNR $\uparrow$	LPIPS $\downarrow$
w/o tri-p.	0.764	25.14	0.287
w/o cont.	0.781	25.34	0.269
w/o tri-p. atte.	0.792	25.59	0.280
full	<b>0.803</b>	<b>25.99</b>	<b>0.266</b>

### 2) Effectiveness of Cross-View Assisted Training Strategy:

In this section, we conduct ablation studies on the proposed Cross-View Stereo Regularization (CVSR) module, Cross-View Augmented Densification (CVAD) module, and Cross-View Consistency Loss (CVCL) module. All modules are implemented using our cross-view assisted training strategy. Furthermore, we specifically optimize the CVCL module through pruning operations. As shown in Table. VI, integrating these key components enables the model to achieve optimal performance, with particularly significant improvements in SSIM metrics. Qualitative results in Fig. 8 demonstrate that incorporating these components significantly enhances rendering quality by improving both detail clarity (e.g., street lamp) and artifact suppression.

TABLE VI  
ABLATION STUDY ON CROSS-VIEW ASSISTED TRAINING STRATEGY.

method	SSIM $\uparrow$	PSNR $\uparrow$	LPIPS $\downarrow$
w/o CVSR	0.741	24.56	0.277
w/o CVAD	0.761	25.04	0.308
w/o $L_{CVC}$	0.780	25.45	0.275
w/o prune	0.780	25.42	0.285
full	<b>0.803</b>	<b>25.99</b>	<b>0.266</b>

3) *Analysis of Hyperparameter Setting:* In this section, we conduct a hyperparameter sensitivity analysis, focusing particularly on examining the impact of parameter  $\tau$  on

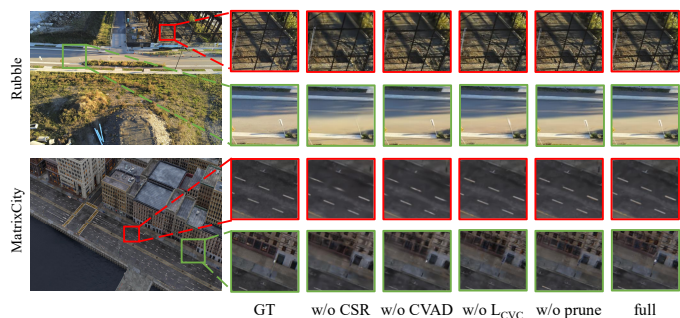


Fig. 8. Qualitative comparison of ablation study on cross-view assisted training strategy. Red & green squares highlight the visual differences for clearer comparison. By reconstructing the fine-grained structures in two scenes, such as the steel frame and signboards in the first row of images, and lane markings and street lamps in the second row of images, we demonstrate the superiority of the comprehensive surface completion training strategy and validate the effectiveness of its individual components. Please *zoom in* to view detailed results.

model performance. As shown in Table. VII, we evaluate five different configurations:  $\tau \in \{0.4, 0.6, 0.8, 1.0, 1.2\}$ . The experimental results demonstrate that the model achieves optimal performance when  $\tau = 1.0$ . This analysis confirms the significant influence of parameter  $\tau$  on the overall method performance.

TABLE VII  
ABLATION STUDY ON THE SETTING OF  $\tau$ .

method	SSIM $\uparrow$	PSNR $\uparrow$	LPIPS $\downarrow$
$\tau=0.4$	0.790	25.81	0.275
$\tau=0.6$	0.792	25.81	0.273
$\tau=0.8$	0.800	25.93	0.269
$\tau=1.0$	<b>0.803</b>	<b>25.99</b>	<b>0.266</b>
$\tau=1.2$	0.802	25.88	0.271

## VI. CONCLUSION AND FUTURE WORK

In this paper, we introduce SplatCo, a structure-view collaborative Gaussian splatting framework designed for high-fidelity, large-scale unbounded scene rendering. We present a cross-structure collaboration module that synergistically fuses

global tri-plane context with local grid features via hierarchical compensation, overcoming detail loss inherent in simpler representations. Then, we propose a cross-view assisted training strategy using gradient consensus and visibility-aware densification to address single-view overfitting and under-reconstruction issues prevalent in sparse large-scale captures, which stems from optimizing Gaussians based on individual viewpoints without explicit cross-view constraints. Furthermore, we enhance geometric integrity and generalization across views through a structural-consistency-guided pruning mechanism. Extensive experiments on 13 diverse large-scale scenes demonstrate the superiority of our approach in rendering quality and detail preservation compared to state-of-the-art methods.

**Limitations:** While the SplatCo method substantially improves detail and consistency in 3D reconstructions, its performance and practical application are subject to certain limitations. These limitations, however, also highlight critical avenues for future methodological enhancements.

Firstly, the efficacy of SplatCo remains sensitive to the input data characteristics. The initial quality of camera poses is a significant factor, as substantial inaccuracies can hinder optimal convergence. Furthermore, the density and overlap of viewpoints are crucial; in scenarios with sparse or irregularly distributed cameras, establishing a robust cross-view consensus becomes intrinsically challenging, which can, in turn, diminish the performance gains typically achieved by the method.

Secondly, our approach’s reliance on joint structure-view optimization, which fundamentally differs from methods that optimize only local representations (like context grids alone) or single global structures (such as basic tri-planes), introduces increased computational overhead. This is primarily due to the demands of multi-view gradient synchronization and the processing of hierarchical features, rendering the method more resource-intensive.

Consequently, addressing these aspects defines critical avenues for future work. There is a clear need for optimizing the trade-off between reconstruction fidelity and computational cost, particularly when operating under demanding capture conditions such as highly non-uniform sampling or significant viewpoint disparity. Future methodological enhancements should therefore include the development of more adaptive view sampling strategies. Additionally, creating lightweight mechanisms for enforcing cross-view consistency will be pivotal in bolstering efficiency without a concomitant sacrifice in the quality of the reconstruction.

## REFERENCES

- [1] R. Martin-Brualla, N. Radwan, M. S. Sajjadi, J. T. Barron, A. Dosovitskiy, and D. Duckworth, “Nerf in the wild: Neural radiance fields for unconstrained photo collections,” in *Proceedings of the IEEE/CVF conference on computer vision and pattern recognition*, 2021, pp. 7210–7219.
- [2] J. Leng, L. Wang, X. Liu, X. Shi, and M. Wang, “Efficient flower text entry in virtual reality,” *IEEE Transactions on Visualization and Computer Graphics*, vol. 28, no. 11, pp. 3662–3672, 2022.
- [3] Y. Hou, C. Wang, J. Wang, X. Xue, X. L. Zhang, J. Zhu, D. Wang, and S. Chen, “Visual evaluation for autonomous driving,” *IEEE Transactions on Visualization and Computer Graphics*, vol. 28, no. 1, pp. 1030–1039, 2021.
- [4] A. Wentzel, S. Attia, X. Zhang, G. Canahuate, C. D. Fuller, and G. E. Marai, “Ditto: A visual digital twin for interventions and temporal treatment outcomes in head and neck cancer,” *IEEE transactions on visualization and computer graphics*, 2024.
- [5] A. W. Harbaugh, *MODFLOW-2005, the US Geological Survey modular ground-water model: the ground-water flow process*. US Department of the Interior, US Geological Survey Reston, VA, USA, 2005, vol. 6.
- [6] V. Croce, E. S. Malinverni, R. Pierdicca, M. Paolanti, E. Frontoni, F. Di Stefano, S. Pansoni, S. Tiribelli, E. S. Malinverni, and B. Giovanola, “Neural radiance fields (nerf) for multi-scale 3d modeling of cultural heritage artifacts,” in *29th CIPA Symposium*, 2024.
- [7] B. Kerbl, G. Kopanas, T. Leimkühler, and G. Drettakis, “3d gaussian splatting for real-time radiance field rendering,” *ACM Trans. Graph.*, vol. 42, no. 4, pp. 139–1, 2023.
- [8] M. Wu and T. Tuytelaars, “Implicit gaussian splatting with efficient multi-level tri-plane representation,” *arXiv preprint arXiv:2408.10041*, 2024.
- [9] Z.-X. Zou, Z. Yu, Y.-C. Guo, Y. Li, D. Liang, Y.-P. Cao, and S.-H. Zhang, “Triplane meets gaussian splatting: Fast and generalizable single-view 3d reconstruction with transformers,” in *Proceedings of the IEEE/CVF conference on computer vision and pattern recognition*, 2024, pp. 10 324–10 335.
- [10] Y. Wang, Z. Li, L. Guo, W. Yang, A. Kot, and B. Wen, “Contextgs: Compact 3d gaussian splatting with anchor level context model,” *Advances in neural information processing systems*, vol. 37, pp. 51 532–51 551, 2024.
- [11] J. Guo, H. Xiao, and W. Kang, “Ea-3dgs: Efficient and adaptive 3d gaussians with highly enhanced quality for outdoor scenes,” *arXiv preprint arXiv:2505.10787*, 2025.
- [12] K. Ren, L. Jiang, T. Lu, M. Yu, Z. Ni, and B. Dai, “Octree-gs: Towards consistent real-time rendering with lod-structured 3d gaussians,” *arXiv preprint arXiv:2403.17898*, 2024.
- [13] H. Cui, X. Gao, S. Shen, and Z. Hu, “Hsfm: Hybrid structure-from-motion,” in *Proceedings of the IEEE conference on computer vision and pattern recognition*, 2017, pp. 1212–1221.
- [14] J. L. Schonberger and J.-M. Frahm, “Structure-from-motion revisited,” in *Proceedings of the IEEE conference on computer vision and pattern recognition*, 2016, pp. 4104–4113.
- [15] L. Zheng, Y. Yang, and Q. Tian, “Sift meets cnn: A decade survey of instance retrieval,” *IEEE transactions on pattern analysis and machine intelligence*, vol. 40, no. 5, pp. 1224–1244, 2017.
- [16] S. Agarwal, N. Snavely, S. M. Seitz, and R. Szeliski, “Bundle adjustment in the large,” in *Computer Vision—ECCV 2010: 11th European Conference on Computer Vision, Heraklion, Crete, Greece, September 5–11, 2010, Proceedings, Part II 11*. Springer, 2010, pp. 29–42.
- [17] S. Galliani, K. Lasinger, and K. Schindler, “Massively parallel multiview stereopsis by surface normal diffusion,” in *Proceedings of the IEEE international conference on computer vision*, 2015, pp. 873–881.
- [18] K. Chen, Z. Yuan, H. Xiao, T. Mao, and Z. Wang, “Learning multi-view stereo with geometry-aware prior,” *Authorea Preprints*, 2025.
- [19] F. Hou, C. Wang, W. Wang, H. Qin, C. Qian, and Y. He, “Iterative poisson surface reconstruction (ipsr) for unoriented points,” *ACM Trans. Graph.*, vol. 41, no. 4, 2022.
- [20] R. Xu, Z. Dou, N. Wang, S. Xin, S. Chen, M. Jiang, X. Guo, W. Wang, and C. Tu, “Globally consistent normal orientation for point clouds by regularizing the winding-number field,” *ACM Trans. Graph.*, vol. 42, no. 4, 2023.
- [21] W. Liu, J. Li, X. Chen, F. Hou, S. Xin, X. Wang, Z. Wu, C. Qian, and Y. He, “Diffusing winding gradients (DWG): A parallel and scalable method for 3d reconstruction from unoriented point clouds,” *ACM Trans. Graph.*, vol. 44, no. 2, 2025.
- [22] S. Lin, Z. Shi, and Y. Liu, “Fast and globally consistent normal orientation based on the winding number normal consistency,” *ACM Trans. Graph.*, vol. 43, no. 6, 2024.
- [23] M. Kazhdan, M. Bolitho, and H. Hoppe, “Poisson surface reconstruction,” in *Proceedings of the Fourth Eurographics Symposium on Geometry Processing*, 2006, pp. 61–70.
- [24] M. Kazhdan and H. Hoppe, “Screened poisson surface reconstruction,” *ACM Trans. Graph.*, vol. 32, no. 3, 2013.
- [25] Y. Yao, Z. Luo, S. Li, T. Fang, and L. Quan, “Mvsnet: Depth inference for unstructured multi-view stereo,” in *European conference on computer vision*, 2018, pp. 767–783.
- [26] X. Wang, Z. Zhu, G. Huang, F. Qin, Y. Ye, Y. He, X. Chi, and X. Wang, “Mvster: Epipolar transformer for efficient multi-view stereo,” in *European conference on computer vision*. Springer, 2022, pp. 573–591.

- [27] Y. Yao, Z. Luo, S. Li, T. Shen, T. Fang, and L. Quan, "Recurrent mvsnet for high-resolution multi-view stereo depth inference," in *Proceedings of the IEEE/CVF conference on computer vision and pattern recognition*, 2019, pp. 5525–5534.
- [28] X. Gu, Z. Fan, S. Zhu, Z. Dai, F. Tan, and P. Tan, "Cascade cost volume for high-resolution multi-view stereo and stereo matching," in *Proceedings of the IEEE/CVF conference on computer vision and pattern recognition*, 2020, pp. 2495–2504.
- [29] Y. Ding, W. Yuan, Q. Zhu, H. Zhang, X. Liu, Y. Wang, and X. Liu, "Transmvsnet: Global context-aware multi-view stereo network with transformers," in *Proceedings of the IEEE/CVF conference on computer vision and pattern recognition*, 2022, pp. 8585–8594.
- [30] W. Gu, H. Xiao, X. Zhao, and W. Kang, "Ea-mvsnet: learning error-awareness for enhanced multi-view stereo," *IEEE Transactions on Circuits and Systems for Video Technology*, 2024.
- [31] S. Wang, V. Leroy, Y. Cabon, B. Chidlovskii, and J. Revaud, "Dust3r: Geometric 3d vision made easy," in *Proceedings of the IEEE/CVF Conference on Computer Vision and Pattern Recognition*, 2024, pp. 20 697–20 709.
- [32] V. Leroy, Y. Cabon, and J. Revaud, "Grounding image matching in 3d with mast3r," in *European Conference on Computer Vision*. Springer, 2024, pp. 71–91.
- [33] J. Yang, A. Sax, K. J. Liang, M. Henaff, H. Tang, A. Cao, J. Chai, F. Meier, and M. Feiszli, "Fast3r: Towards 3d reconstruction of 1000+ images in one forward pass," *arXiv preprint arXiv:2501.13928*, 2025.
- [34] J. Han, H. An, J. Jung, T. Narihira, J. Seo, K. Fukuda, C. Kim, S. Hong, Y. Mitsufuji, and S. Kim, "D<sup>2</sup>ust3r: Enhancing 3d reconstruction with 4d pointmaps for dynamic scenes," *arXiv preprint arXiv:2504.06264*, 2025.
- [35] W. Liu, Z. Piao, J. Min, W. Luo, L. Ma, and S. Gao, "Liquid warping gan: A unified framework for human motion imitation, appearance transfer and novel view synthesis," in *Proceedings of the IEEE/CVF international conference on computer vision*, 2019, pp. 5904–5913.
- [36] Y.-C. Guo, Y.-P. Cao, C. Wang, Y. He, Y. Shan, and S.-H. Zhang, "Vmesh: Hybrid volume-mesh representation for efficient view synthesis," in *SIGGRAPH Asia 2023 Conference Papers*, 2023, pp. 1–11.
- [37] J. Sun, Z. Zhang, J. Chen, G. Li, B. Ji, L. Zhao, W. Xing, and H. Lin, "Vgos: Voxel grid optimization for view synthesis from sparse inputs," *arXiv preprint arXiv:2304.13386*, 2023.
- [38] K. Schwarz, A. Sauer, M. Niemeyer, Y. Liao, and A. Geiger, "Voxgraf: Fast 3d-aware image synthesis with sparse voxel grids," *Advances in Neural Information Processing Systems*, vol. 35, pp. 33 999–34 011, 2022.
- [39] H. Xiao, Y. Li, W. Kang, and Q. Wu, "Distinguishing and matching-aware unsupervised point cloud completion," *IEEE Transactions on Circuits and Systems for Video Technology*, vol. 33, no. 9, pp. 5160–5173, 2023.
- [40] J. Korhonen, G. Rangu, H. R. Tavakoli, and J. Kannala, "Efficient nerf optimization-not all samples remain equally hard," in *European Conference on Computer Vision*. Springer, 2024, pp. 198–213.
- [41] R. Li, H. Gao, M. Tancik, and A. Kanazawa, "Nerfacc: Efficient sampling accelerates nerfs," in *Proceedings of the IEEE/CVF international conference on computer vision*, 2023, pp. 18 537–18 546.
- [42] J. T. Barron, B. Mildenhall, M. Tancik, P. Hedman, R. Martin-Brualla, and P. P. Srinivasan, "Mip-nerf: A multiscale representation for anti-aliasing neural radiance fields," in *Proceedings of the IEEE/CVF international conference on computer vision*, 2021, pp. 5855–5864.
- [43] D. Hu, Z. Zhang, T. Hou, T. Liu, H. Fu, and M. Gong, "Multiscale representation for real-time anti-aliasing neural rendering," in *Proceedings of the IEEE/CVF International Conference on Computer Vision*, 2023, pp. 17 772–17 783.
- [44] L. Ma, X. Li, J. Liao, Q. Zhang, X. Wang, J. Wang, and P. V. Sander, "Deblur-nerf: Neural radiance fields from blurry images," in *Proceedings of the IEEE/CVF Conference on Computer Vision and Pattern Recognition*, 2022, pp. 12 861–12 870.
- [45] X. Wang, Z. Yin, F. Zhang, D. Feng, and Z. Wang, "Mp-nerf: More refined deblurred neural radiance field for 3d reconstruction of blurred images," *Knowledge-Based Systems*, vol. 290, p. 111571, 2024.
- [46] A. Pumarola, E. Corona, G. Pons-Moll, and F. Moreno-Noguer, "D-nerf: Neural radiance fields for dynamic scenes," in *Proceedings of the IEEE/CVF Conference on Computer Vision and Pattern Recognition*, 2021, pp. 10 318–10 327.
- [47] G. Chen and W. Wang, "A survey on 3d gaussian splatting," 2025. [Online]. Available: <https://arxiv.org/abs/2401.03890>
- [48] B. Fei, J. Xu, R. Zhang, Q. Zhou, W. Yang, and Y. He, "3d gaussian splatting as new era: A survey," *IEEE Transactions on Visualization and Computer Graphics*, 2024.
- [49] T. Wu, Y.-J. Yuan, L.-X. Zhang, J. Yang, Y.-P. Cao, L.-Q. Yan, and L. Gao, "Recent advances in 3d gaussian splatting," *Computational Visual Media*, vol. 10, pp. 613–642, 2024.
- [50] V. Pryadilshchikov, A. Markin, A. Komarichev, R. Rakhimov, P. Wonka, and E. Burnaev, "T-3dgs: Removing transient objects for 3d scene reconstruction," *arXiv preprint arXiv:2412.00155*, 2024.
- [51] X. Sun, J. C. Lee, D. Rho, J. H. Ko, U. Ali, and E. Park, "F-3dgs: Factorized coordinates and representations for 3d gaussian splatting," in *Proceedings of the 32nd ACM International Conference on Multimedia*, 2024, pp. 7957–7965.
- [52] J. Sakamiya, I. Shen, J. Zhang, M. D. Dogan, T. Igarashi *et al.*, "Avatarperfect: User-assisted 3d gaussian splatting avatar refinement with automatic pose suggestion," *arXiv preprint arXiv:2412.15609*, 2024.
- [53] C. Chen, L. Yu, Q. Yang, A. Zheng, and H. Xie, "Thgs: Lifelike talking human avatar synthesis from monocular video via 3d gaussian splatting," in *Computer Graphics Forum*. Wiley Online Library, 2025, p. e15282.
- [54] L. Qiu, S. Zhu, Q. Zuo, X. Gu, Y. Dong, J. Zhang, C. Xu, Z. Li, W. Yuan, L. Bo *et al.*, "Anigs: Animatable gaussian avatar from a single image with inconsistent gaussian reconstruction," *arXiv preprint arXiv:2412.02684*, 2024.
- [55] M. Yu, T. Lu, L. Xu, L. Jiang, Y. Xiangli, and B. Dai, "Gsd: 3dgs meets sdf for improved rendering and reconstruction," *arXiv preprint arXiv:2403.16964*, 2024.
- [56] Q. Wu, J. Zheng, and J. Cai, "Surface reconstruction from 3d gaussian splatting via local structural hints," in *European Conference on Computer Vision*. Springer, 2024, pp. 441–458.
- [57] H. Xiang, X. Li, K. Cheng, X. Lai, W. Zhang, Z. Liao, L. Zeng, and X. Liu, "Gaussianroom: Improving 3d gaussian splatting with sdf guidance and monocular cues for indoor scene reconstruction," 2025. [Online]. Available: <https://arxiv.org/abs/2405.19671>
- [58] T. Lu, M. Yu, L. Xu, Y. Xiangli, L. Wang, D. Lin, and B. Dai, "Scaffold-gs: Structured 3d gaussians for view-adaptive rendering," in *Proceedings of the IEEE/CVF Conference on Computer Vision and Pattern Recognition*, 2024, pp. 20 654–20 664.
- [59] Y. Chen and G. H. Lee, "Dogs: Distributed-oriented gaussian splatting for large-scale 3d reconstruction via gaussian consensus," *Advances in Neural Information Processing Systems*, vol. 37, pp. 34 487–34 512, 2024.
- [60] J. Lin, Z. Li, X. Tang, J. Liu, S. Liu, J. Liu, Y. Lu, X. Wu, S. Xu, Y. Yan *et al.*, "Vastgaussian: Vast 3d gaussians for large scene reconstruction," in *Proceedings of the IEEE/CVF Conference on Computer Vision and Pattern Recognition*, 2024, pp. 5166–5175.
- [61] B. Kerbl, A. Meuleman, G. Kopanas, M. Wimmer, A. Lanvin, and G. Drettakis, "A hierarchical 3d gaussian representation for real-time rendering of very large datasets," *ACM Transactions on Graphics (TOG)*, vol. 43, no. 4, pp. 1–15, 2024.
- [62] Y. Liu, C. Luo, L. Fan, N. Wang, J. Peng, and Z. Zhang, "Citygaussian: Real-time high-quality large-scale scene rendering with gaussians," in *European Conference on Computer Vision*. Springer, 2024, pp. 265–282.
- [63] H. Xiao, H. Xu, Y. Li, and W. Kang, "Multi-dimensional graph interactional network for progressive point cloud completion," *IEEE Transactions on Instrumentation and Measurement*, vol. 72, pp. 1–12, 2022.
- [64] S. Fridovich-Keil, G. Meanti, F. R. Warburg, B. Recht, and A. Kanazawa, "K-planes: Explicit radiance fields in space, time, and appearance," in *Proceedings of the IEEE/CVF Conference on Computer Vision and Pattern Recognition*, 2023, pp. 12 479–12 488.
- [65] S. Woo, J. Park, J.-Y. Lee, and I. S. Kweon, "Cbam: Convolutional block attention module," in *Proceedings of the European conference on computer vision (ECCV)*, 2018, pp. 3–19.
- [66] H. Turki, D. Ramanan, and M. Satyanarayanan, "Mega-nerf: Scalable construction of large-scale nerfs for virtual fly-throughs," in *Proceedings of the IEEE/CVF Conference on Computer Vision and Pattern Recognition*, 2022, pp. 12 922–12 931.
- [67] M. Zhenxing and D. Xu, "Switch-nerf: Learning scene decomposition with mixture of experts for large-scale neural radiance fields," in *The Eleventh International Conference on Learning Representations*, 2022.
- [68] J. Waczyńska, P. Borycki, S. Tadeja, J. Tabor, and P. Spurek, "Games: Mesh-based adapting and modification of gaussian splatting," *arXiv preprint arXiv:2402.01459*, 2024.
- [69] J. C. Lee, D. Rho, X. Sun, J. H. Ko, and E. Park, "Compact 3d gaussian representation for radiance field," in *Proceedings of the IEEE/CVF Conference on Computer Vision and Pattern Recognition*, 2024, pp. 21 719–21 728.

- [70] T. Lu, M. Yu, L. Xu, Y. Xiangli, L. Wang, D. Lin, and B. Dai, "Scaffold-gs: Structured 3d gaussians for view-adaptive rendering," in *Proceedings of the IEEE/CVF Conference on Computer Vision and Pattern Recognition*, 2024, pp. 20 654–20 664.
- [71] Z. Zhang, W. Hu, Y. Lao, T. He, and H. Zhao, "Pixel-gs: Density control with pixel-aware gradient for 3d gaussian splatting," *arXiv preprint arXiv:2403.15530*, 2024.
- [72] Z. Wang, A. C. Bovik, H. R. Sheikh, and E. P. Simoncelli, "Image quality assessment: from error visibility to structural similarity," *IEEE transactions on image processing*, vol. 13, no. 4, pp. 600–612, 2004.
- [73] Y. Li, L. Jiang, L. Xu, Y. Xiangli, Z. Wang, D. Lin, and B. Dai, "Matrixcity: A large-scale city dataset for city-scale neural rendering and beyond," in *Proceedings of the IEEE/CVF International Conference on Computer Vision*, 2023, pp. 3205–3215.
- [74] A. Knapitsch, J. Park, Q.-Y. Zhou, and V. Koltun, "Tanks and temples: Benchmarking large-scale scene reconstruction," *ACM Transactions on Graphics*, vol. 36, no. 4, pp. 1–13, 2017.
- [75] J. Liu and S. Ji, "A novel recurrent encoder-decoder structure for large-scale multi-view stereo reconstruction from an open aerial dataset," in *Proceedings of the IEEE/CVF conference on computer vision and pattern recognition*, 2020, pp. 6050–6059.
- [76] L. Morelli, F. Ioli, R. Beber, F. Menna, F. Remondino, and A. Vitti, "Colmap-slam: A framework for visual odometry," *The International Archives of the Photogrammetry, Remote Sensing and Spatial Information Sciences*, vol. 48, pp. 317–324, 2023.
- [77] R. Zhang, P. Isola, A. A. Efros, E. Shechtman, and O. Wang, "The unreasonable effectiveness of deep features as a perceptual metric," in *Proceedings of the IEEE conference on computer vision and pattern recognition*, 2018, pp. 586–595.
- [78] J. T. Barron, B. Mildenhall, D. Verbin, P. P. Srinivasan, and P. Hedman, "Mip-nerf 360: Unbounded anti-aliased neural radiance fields," in *Proceedings of the IEEE/CVF conference on computer vision and pattern recognition*, 2022, pp. 5470–5479.
- [79] T. Müller, A. Evans, C. Schied, and A. Keller, "Instant neural graphics primitives with a multiresolution hash encoding," *ACM transactions on graphics (TOG)*, vol. 41, no. 4, pp. 1–15, 2022.
- [80] S. Fridovich-Keil, A. Yu, M. Tancik, Q. Chen, B. Recht, and A. Kanazawa, "Plenoxels: Radiance fields without neural networks," in *Proceedings of the IEEE/CVF conference on computer vision and pattern recognition*, 2022, pp. 5501–5510.